JOURNAL OF SPACECRAFT AND ROCKETS
Vol. 38, No. 5, September–October 2001

X-33 Hypersonic Aerodynamic Characteristics

Kelly J. Murphy,* Robert J. Nowak,† Richard A. Thompson,* and Brian R. Hollis†
NASA Langley Research Center, Hampton, Virginia 23681
and
Ramadas Prabhu‡
Lockheed Martin Engineering and Sciences, Hampton, Virginia 23681

Lockheed Martin Skunk Works, under a cooperative agreement with NASA, will design, build, and fly the X-33, a half-scale prototype of a rocket-based, single-stage-to-orbit, reusable launch vehicle. A 0.007-scale model of the X-33 604B0002G configuration was tested in five supersonic/hypersonic facilities at the NASA Langley Research Center to examine vehicle aerodynamic characteristics and to establish the aerodynamic flight database for the hypersonic regime. Effects of Mach number and specific heat ratio on hypersonic aerodynamic characteristics were also studied. These results were complemented with computational aerodynamic data, experimental configuration buildup information, and various types of surface and flowfield visualizations to enhance the understanding of experimentally observed aerodynamic trends. Data at both Mach 6 and Mach 10 show the baseline configuration achieves a maximum hypersonic *L/D* of approximately 1.2 between 20 and 30 deg angle of attack. With the center-of-gravity location at 66% of vehicle reference length, the configuration was found to be longitudinally controllable with less than half of the total body flap deflection capability across the angle of attack range at both Mach 6 and Mach 10. The vehicle also was shown to be longitudinally stable or neutrally stable for typical (greater than 20 deg) hypersonic flight attitudes. At Mach 6 and Mach 10, the baseline configuration demonstrated positive dihedral effect (roll stability) but was directionally unstable. Effects of Mach number on longitudinal aerodynamics were shown to be small relative to X-33 control authority. Effects of specific heat ratio on vehicle pitching moment characteristics were shown to be significant at higher angles of attack, but with a maximum flight Mach number of approximately 10, real-gas phenomena are not expected to occur for the X-33's suborbital flights.

Nomenclature

B_{ref}	=	lateral reference length, ft or in.
C_A	=	axial-force coefficient
C_D	=	drag-force coefficient
C_L	=	lift-force coefficient
C_{La}	=	lift curve slope, $dC_L/d\alpha$
C_{L0}	=	lift-force coefficient at 0-deg angle of attack
C_l	=	rolling-moment coefficient
$C_{l\beta}$	=	rolling-moment beta derivative, $dC_l/d\beta$
C_m	=	pitching-moment coefficient
$C_{m\alpha}$	=	pitching-moment alpha derivative, $dC_m/d\alpha$
C_N	=	normal-force coefficient
C_n	=	yawing-moment coefficient
$C_{n\beta}$	=	yawing-moment beta derivative, $dC_n/d\beta$
C_Y	=	side-force coefficient
L_{ref}	=	longitudinal reference length, ft or in.
M	=	Mach number
P_t	=	tunnel stagnation pressure, psia
P_∞	=	freestream static pressure, psia
q_∞	=	freestream dynamic pressure, psia
Re_∞	=	freestream unit Reynolds number, per ft
$S_{\text{canted fin}}$	=	canted fin reference area, ft^2 or in.^{2}
S_{elevon}	=	elevon reference area, ft^2 or in.^{2}
S_{flap}	=	body flap reference area, ft^2 or in.^{2}
S_{ref}	=	vehicle reference area, ft^2 or in.^{2}
$S_{\text{vertical fin}}$	=	vertical fin reference area, ft^2 or in.^{2}
T_∞	=	freestream static temperature, °R
T_t	=	tunnel stagnation temperature, °R
α	=	angle of attack, deg
β	=	angle of sideslip, deg
γ_2	=	postshock ratio of specific heats
γ_∞	=	freestream ratio of specific heats
ΔC_m	=	increment in pitching-moment coefficient
$\Delta C_{m\,\text{bf}}$	=	increment in pitching-moment coefficient due to body flap
$\Delta C_{m\,\text{el}}$	=	increment in pitching-moment coefficient due to elevon
δ_{bf}	=	body flap deflection, deg
δ_{el}	=	elevon deflection, deg
ρ_2/ρ_∞	=	shock density ratio

Received 3 December 1999; revision received 7 November 2000; accepted for publication 15 February 2001.

*Aerospace Technologist, Aerothermodynamics Branch, Aerodynamics, Aerothermodynamics, and Acoustics Competency.
†Aerospace Technologist, Aerothermodynamics Branch, Aerodynamics, Aerothermodynamics, and Acoustics Competency. Member AIAA.
‡Senior Aerospace Engineer, Langley Program Office.

Introduction

AS a first step toward development of an operational next-generation reusable launch system, Lockheed Martin Skunk Works (LMSW), under a cooperative agreement with NASA, will design, build, and fly the X-33, a half-scale prototype of a rocket-based, single-stage-to-orbit (SSTO), reusable launch vehicle (RLV). The objective of the X-33 program is to develop and demonstrate key design and operational aspects of an SSTO vehicle to reduce the business and technical risks to the private sector in developing a commercially viable RLV system. The X-33 concept has a lifting body shape with two integrated linear aerospike rocket engines and flies a suborbital trajectory to simulate important aerodynamic and aerothermodynamic aspects of ascent and reentry environments for a full-scale RLV. For its initial flights, the X-33 vehicle will be launched vertically from a site at Edwards Air Force Base in southern California and land horizontally at Michael Air Force Base in Utah. Multiple flights are planned to examine vehicle aerodynamic and structural characteristics, thermal protection system (TPS) robustness, and engine performance to validate new technologies with scalability and traceability to a future RLV.

At the beginning of this decade, the National Aerospace Plane (NASP/X-30) was an SSTO concept studied by both the Department of Defense and NASA. The NASP configuration was a form of lifting body[1] with an integrated hypersonic airbreathing propulsion system. The program was terminated in 1994 when it was

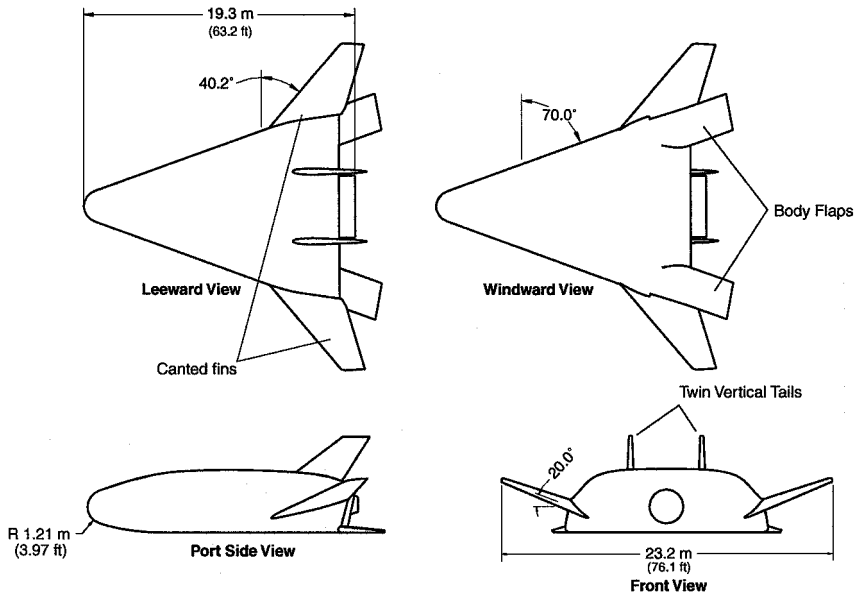

Fig. 1 Full-scale X-33 604B0002F/G configuration.

realized that the high-temperature materials and airbreathing propulsion technology necessary to fly the X-30 would take many more years to mature. Based on the Access to Space Study[2] that followed the termination of the X-30 program, NASA moved forward to develop, in partnership with private industry, a rocket-based, SSTO, fully RLV system. NASA solicited proposals from the aerospace industry in 1994 to design and build the X-33, an advanced technology demonstrator that would lead to development of a SSTO RLV system that would begin flying in the 2005 time frame. Three companies, Lockheed Martin, McDonnell Douglas, and Rockwell International submitted competitive configurations for the X-33. For 15 months beginning in the Spring of 1995, personnel in NASA Langley Research Center Aerothermodynamics Branch led an intensive testing and evaluation effort of the three concepts, designated as phase I of the X-33 program. Aerodynamic performance and aeroheating were assessed in the relevant speed regimes for all three configurations. This work resulted in significant changes in outer-mold-line geometry from initial phase I designs. Based on information obtained in phase I, the three companies were required to submit proposals for evaluation, which contained both the technical and financial feasibility of their configurations. On 2 July 1996, it was announced that the LMSW had been selected to build and fly the X-33.

The X-33 vehicle, currently being built by LMSW in Palmdale, California, is a 63-ft-long lifting body with 20-deg-dihedral canted fins, two windward side body flaps, and twin vertical tails (Fig. 1). The maximum body span between canted fin tips is 76 ft. The external body shape is defined by the internal fuel tank structure; a single liquid oxygen tank defines the forward portion of the body and a dual-lobed liquid hydrogen tank defines the aft portion of the vehicle. Two linear aerospike engines will propel the vehicle to Mach numbers of 10 or greater. The vehicle will be protected from intense aeroheating by a windward array of metallic panels. The hydrogen fuel tank design, linear-aerospike engines, and metallic TPS all represent significant technical challenges for this configuration, and if proven successful in flight testing, these technologies could be critical to SSTO feasibility.

The X-33, designed to be a suborbital vehicle, is to be launched from a newly constructed launch site within Edwards Air Force Base in southern California. On its first flights, the X-33 will accelerate to a maximum Mach number of 10, fly to a maximum altitude of 180,000 ft, and land at Michael Air Force Base in Utah. A typical X-33 trajectory to Michael is shown in Fig. 2. The vehicle's design envelope includes a more aggressive trajectory to Malstrom Air Force Base in Montana, flying up to Mach 15 and 250,000 ft, but current vehicle performance estimates make this trajectory a less likely candidate unless flight tests show significantly increased

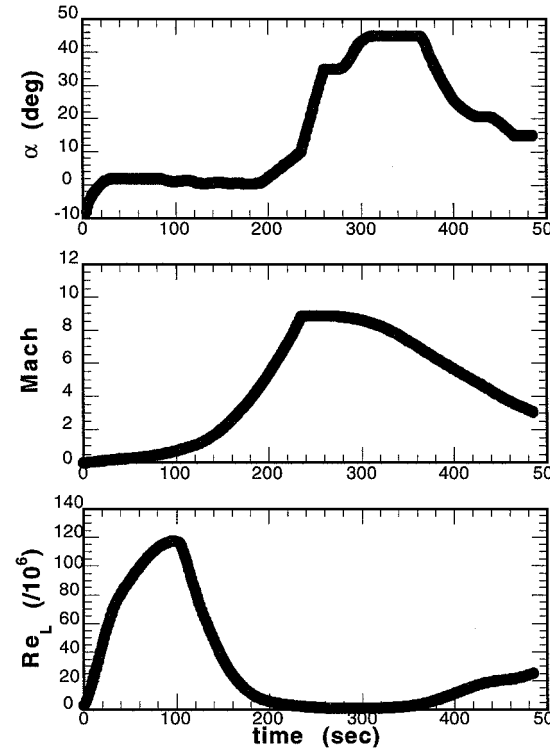

Fig. 2 Typical X-33 trajectory parameters.

performance. Multiple flights are planned to examine vehicle aerodynamic and structural characteristics, TPS robustness, and engine performance to validate new technologies with scalability and traceability to a future RLV.

Objectives

Phase II of the X-33 program began with the selection of the LMSW X-33 concept. In support of specified developmental task agreements, testing began at NASA Langley Research Center in the late fall of 1996 in the areas of aerodynamics, aeroheating, and structures and materials. This report presents results generated by the authors in support of phase II X-33 in the area of experimental hypersonic aerodynamics. To provide Lockheed with necessary aerodynamic data in this fast-paced program, a subscale model of the X-33 was designed, fabricated, and tested in several supersonic/hypersonic wind tunnels at the NASA Langley Research

Center over a 12-month period, and the data were rapidly reduced, analyzed, and disseminated.

The test program described in this paper was designed to satisfy three primary objectives: 1) The first is to provide benchmark aerodynamic data in the hypersonic speed regime to populate the X-33 flight database. To accomplish this first objective, a 0.007-scale stainless steel X-33 force and moment model was fabricated for testing in the Aerothermodynamics Facilities Complex (AFC) at NASA Langley Research Center (LaRC). The primary facility used for generating benchmark hypersonic aerodynamic data was the 20-Inch Mach 6 Air Tunnel. An extensive matrix of six-component force and moment data were taken on the X-33 model using different strain-gauge force balances and support systems to establish data credibility. Nearly 400 runs were made in the 20-Inch Mach 6 Air Tunnel to characterize baseline vehicle stability and control and performance characteristics and to quantify body flap and elevon control authority at relevant angles of attack and sideslip. 2) The second objective is to examine, where possible, effects of compressibility and real-gas phenomenon on X-33 hypersonic aerodynamic characteristics. This second objective required testing the 0.007-scale force-and-moment model at different Mach numbers and postshock specific heat ratios. To study compressibility effects, the 0.007-scale model was tested in the LaRC 31-Inch Mach 10 Air Tunnel and the data compared to that obtained at Mach 6 for the same value of Reynolds number. To investigate so-called real-gas effects, the 0.007-scale model was tested in the LaRC 20-Inch Mach 6 CF_4 Tunnel, a facility that simulates a lower postshock specific heat ratio (associated with a dissociated flow within the shock layer at hypervelocity flight conditions) by using a heavy gas as the test medium and comparing CF_4 and air results for Mach 6. 3) The third objective is to provide complementary experimental and computational data to the hypersonic aerodynamic database to enhance understanding of observed aerodynamic characteristics of the X-33 configuration. To address this third objective, additional visualization techniques were used, inviscid and viscous hypersonic computational fluid dynamics CFD codes were exercised, and a complementary configuration buildup study was conducted.

Experimental Program

Model Description

All experimental aerodynamic data presented in this report were obtained with a 0.007-scale metallic force-and-moment model designed and fabricated in-house at LaRC. The outer-mold-line (OML) geometry was obtained from LMSW and is designated as the 604B0002G configuration. The 604B0002G OMLs were similar to those of the 604B0002F (also referred to as Rev F) configuration, which was used to generate the aeroheating database for the X-33,[3,4] the only difference being minor modifications to the small protrusions on the aft upper surface of the vehicle and the canted fin body fillet.[5] The reference areas and lengths used to calculate aerodynamic coefficient data for the full-scale vehicle and the 0.007-scale model are presented in Table 1.

All model components (except aluminum canted fin offblocks) were fabricated from stainless steel and included removable canted fins, body flaps, vertical tails, and engine blocks. Rudder and elevon deflections were integral to the vertical tails and canted fins, respectively, and thus, numerous fins and tails were made to accommodate required control surface deflections. Body flap deflections were obtained by using individually machined tabbed flaps with the given deflection. Fin, flap, and engine offblocks were machined and fitted to the model for configuration buildup studies. The model's body

Table 1 Reference dimensions

Dimension	Full scale	0.007-scale
S_{ref}	1608 ft^2	11.346 in.^{2}
L_{ref}	63.2 ft	5.309 in.
B_{ref}	36.6 ft	3.074 in.
S_{flap} (total)	164 ft^2	1.157 in.^{2}
$S_{canted\ fin}$ (total)	376 ft^2	2.653 in.^{2}
S_{elevon} (total)	86.4 ft^2	0.6096 in.^{2}
$S_{vertical\ fin}$ (total)	170 ft^2	1.200 in.^{2}
c.g.$_{ref}$ (66% L_{ref})	41.7 ft	3.506 in.

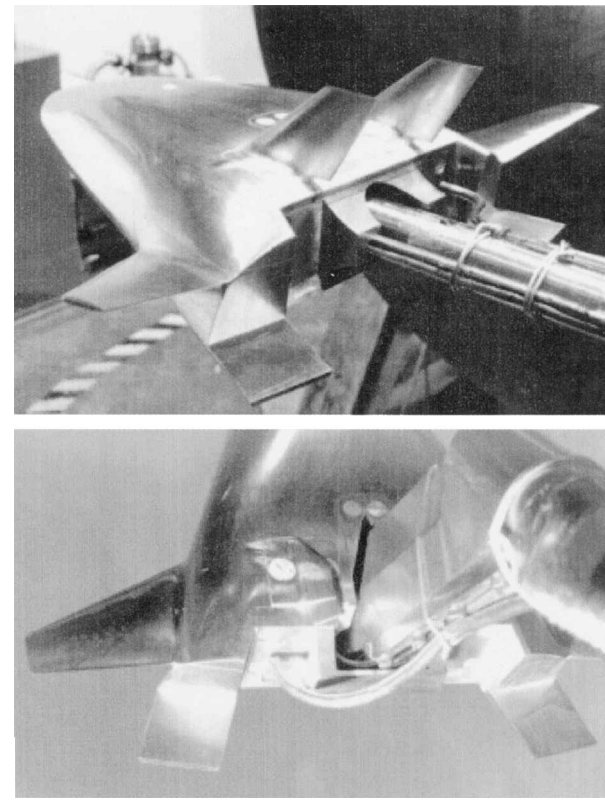

Fig. 3 Installation of 0.7% X-33 on sting (top) and blade (bottom) mounts in 31-Inch Mach 10 tunnel.

and base section were designed in such a way as to receive either a straight sting or a 30-deg blade strut support. The blade, designed for use at higher angles of attack, exits the leeside of the model. This allows the windward side of the linear aerospike engine nozzle to be preserved. The $\frac{1}{2}$-in.-diam straight sting significantly impacts base region nozzle geometry, but preserves the model's leeside geometry. Different facilities permitted varying degrees of overlap in the angle-of-attack range for the blade and sting supports. Photographs of the baseline model, sting and blade mounted, are shown in Fig. 3.

The OMLs of the X-33 hypersonic aerodynamic model were extensively checked against X-33 geometry files by LaRC Surface Verification Laboratory. The x, y, z location of over 4500 surface contour points were measured to characterize model quality: 60% of measured contour points were within ± 0.003 in tolerance, 93% of measured contour points were within ± 0.006 in tolerance, and over 99% of measured contour points were within ± 0.009 in. These surface measurements were also used to determine precisely balance bore alignment and balance electrical center location for accurate calculation of model attitude and moment transfer distances.

Facility Description

All hypersonic data generated in phase II X-33 testing were obtained in four facilities in LaRC AFC. The AFC consists of five blowdown-to-vacuum, conventional- (as opposed to impulse-) type wind tunnels that provide a wide range of flow simulation parameters. Three different test gases are used as flow media: air, helium (He), and tetrafluoromethane (CF_4). The AFC facilities used for X-33 aerodynamic testing were the 20-Inch Mach 6 Air Tunnel (referred to as the Mach 6 tunnel), the 31-Inch Mach 10 Air Tunnel (referred to as the Mach 10 tunnel), the 20-Inch Mach 6 CF_4 Tunnel (referred to as the CF_4 tunnel), and the 22-Inch Mach 20 Helium Tunnel (referred to as the helium tunnel). Data obtained in the Mach 6 and Mach 10 tunnels allow examination of the effect of increasing Mach number (compressibility effects) on the aerodynamic coefficients. Comparisons of data between the Mach 6 air and CF_4 tunnels provide, through a decrease in specific heat ratio from 1.4 in air to 1.15 in CF_4 (for flow within the shock layer of models), an indication of the significance of so-called real-gas effects for the configuration. Because of low stagnation temperatures,

Table 2 Nominal flow conditions

Facility	Mach	q_∞, psi	P_t, psi	T_t, °R	Re/ft
20-Inch Mach 6 air	6	2.0	125	910	2.0
31-Inch Mach 10 air	10	2.2	1450	1800	2.2
20-Inch Mach 6 CF_4	6[a]	0.9	950	1150	0.4
22-Inch Mach 20 He	20	1.7	1000	530	7.5
UPWT leg II air	4.63	1.5	35	610	2.0

[a]Mach 13–18 simulation due to increased ρ_2/ρ_∞.

hypersonic data can be obtained in the helium tunnel very rapidly on plastic models, and thus, this facility was used generate the initial hypersonic data on the X-33 configuration. Additional high supersonic aerodynamic data were obtained in leg II of LaRC's Unitary Plan Wind Tunnel (UPWT) to complement the hypersonic database generated in the AFC. The history and capabilities of the AFC and the UPWT are thoroughly discussed in Refs. 6 and 7. A brief description of each facility utilized for this study will be presented in the sections that follow, and nominal flow conditions for the tests run can be found in Table 2.

20-Inch Mach 6 Tunnel

This facility, which became operational in 1958, is a blowdown wind tunnel that uses heated, dried, filtered air as the test gas. A fixed-geometry, two-dimensional contoured nozzle is used to generate Mach 6 flow in a test section with 20.5 × 20 in. cross section. Typical run times are 2–10 min, depending on the requirements of the study and the tunnel running conditions. The tunnel can operate at stagnation pressures from 30 to 500 psi and stagnation temperatures from 750 to 1000 °R, corresponding to freestream Mach numbers from 5.8 to 6.1 and unit Reynolds numbers from 0.5×10^6 to 9×10^6/ft. Test core size, as defined by a maximum of ±1.0% variation in pitot pressure, varies from approximately 12 × 12 in. to 14 × 14 in. as freestream Reynolds number increases. The normal shock density ratio for this facility is 5.3, and ideal-gas behavior is achieved within the entire flow sequence, that is, $\gamma = 1.4$ everywhere. Models are mounted on an injection system located in a housing below the closed test section. A computer-operated sting support system is capable of moving the model through an angle-of-attack range from −5 to +55 deg for angles of sideslip from 0 to ±10 deg. Model injection times can be as rapid as 0.5 s (commonly used for heat transfer tests), but generally are set for 1.2 s to keep model acceleration less than 2 g to avoid damage to the force balances.

31-Inch Mach 10 Tunnel

Although designed in the 1950s as a blowdown starting, continuously running facility, the Mach 10 tunnel now operates solely in a blowdown mode and uses heated, dried, filtered air as the test gas. The facility uses a three-dimensional contoured nozzle with a 1.07-in. square throat and a 31-in. square test section. The Mach 10 tunnel has been calibrated for reservoir pressures from 350 to 1450 psia for a stagnation temperature of approximately 1800 °R, which corresponds to a range of freestream unit Reynolds numbers of 0.5×10^6 to 2.1×10^6/ft. The test core varies from about 12 × 12 in at the lowest Reynolds number condition to approximately 14 × 14 in at the highest value. (Note that core size is the same as for the Mach 6 tunnel.) For aerodynamic testing, models are kept within a ±7 in inviscid test core where the pitot pressure distribution varies less than ±1.0%. The normal shock density ratio for this facility is 5.9, which is naturally higher than the Mach 6 facility and higher than perfect-air predictions ($\rho_2/\rho_\infty = 5.74$ for $M_\infty = 10$) due to vibrational excitation associated with the higher temperatures in this facility. The Mach 10 tunnel can achieve run times of approximately 120 s. Models are supported on a hydraulically operated, sidewall-mounted injection system and can be injected to the nozzle centerline in less than 0.6 s (an injection time of 2 s is used for force and moment testing). The computer-controlled support strut is able to achieve a pitch range from −10 to +45 deg and a sideslip range of ±5 deg.

20-Inch Mach 6 CF_4 Tunnel

The LaRC 20-Inch Mach 6 CF_4 Tunnel is the only known low-enthalpy, hypersonic wind tunnel in the country that generates a normal shock density ratio approaching that experienced during the hypervelocity portion of reentry into the Earth's atmosphere. This facility uses a test gas three times heavier than air, CF_4, with a lower corresponding γ_∞ (1.22) than ideal air to simulate the reduced γ, and increased ρ_2/ρ_∞, of a real gas due to dissociation in the shock layer. (Note that actual real-gas chemistry is not simulated in this facility.) Because of the increased shock density ratio, a Mach 6 condition in CF_4 provides a Mach 13–18 flight simulation for Earth entry. CF_4 test gas is expanded through an axisymmetric contoured nozzle having a throat diameter of 0.446 in. and an exit diameter of 20 in. and designed to produce Mach 6 at the exit. The tunnel has been calibrated for reservoir pressures from 100 to 2000 psia and temperatures from 1100 to 1400 °R, corresponding to a normal shock density ratio of 12 at Mach 6 and a range of unit Reynolds numbers from 0.05×10^6 to 0.7×10^6/ft. Within the open jet test section, pitot pressure is observed to vary approximately ±1.0% across the test core, with the exception of a 1-in. diameter around the tunnel centerline, where the variation increases to ±3.0% due to a centerline disturbance (typical of axisymmetric contoured nozzles). Models are supported at the nozzle exit by a hydraulically driven injection mechanism for which the angle of attack may be varied from −10 to +50 deg and the angle of sideslip from −5 to +5 deg. The injection time is variable from approximately 0.5 s for heat transfer tests to 2 s for force and moment tests.

22-Inch Mach 20 He Tunnel

Similar to the CF_4 Tunnel, the LaRC 22-Inch Mach 20 Helium Tunnel provides a hypersonic test capability unique in the country. The helium tunnel is the only high hypersonic Mach number facility for which the freestream flow and flow within the shock layer of a model are everywhere thermally and calorically perfect. This results from the helium test gas not requiring heating because it may be expanded to temperatures as low as 3 to 4 °R without liquefying at the corresponding low pressures. An important byproduct of the facility's low stagnation temperatures is that rapid prototype plastic or wooden models may be used for testing, making this a valuable facility for initial hypersonic screening. The helium tunnel is a closed-cycle, blowdown facility that uses purified helium, stored in a 5000-psia storage system. Helium gas is expanded through 0.622-in.-diam throat and an axisymmetric contoured nozzle, designed to provide Mach 20 at the exit, into a contoured test section having a maximum diameter of 22 in. Calibration results exist for ambient temperatures and a range of reservoir pressures from 500 to 1500 psia, corresponding to a variation in Reynolds numbers from 4.0×10^6 to 11.3×10^6/ft. The freestream ratio of specific heats is 1.67, and the shock density ratio is 4 (lower than the 5.3 value for Mach 6 perfect-gas airflow). The test section is equipped with a hydraulically driven model injection system capable of producing pitch variations from −10 to +50 deg and sideslip variations of ±5 deg. Typical injection time is approximately 2 s, and typical run times are on the order of 30 s.

UPWT-Leg II

The UPWT is a closed-circuit, continuous-running pressure tunnel with two test sections that are nominally 4 × 4 ft in cross section and 7 ft long. The stagnation pressure can be varied up to a maximum of approximately 50 psia in test section I and approximately 100 psia in test section II. The nozzle throat-to-test-section area ratio is varied by a lower asymmetric sliding nozzle block that provides continuous variation of the Mach number. The Mach number range is nominally 1.5 to 2.86 in test section I and 2.3 to 4.63 in test section II. Tunnel stagnation temperatures are typically 125 and 150°F for each test section, respectively. Reynolds numbers from 1.0×10^6 to 5.0×10^6/ft can be run routinely with a capability to reach 6.0×10^6/ft on a transient basis. The basic model support mechanism is a horizontal wall-mounted strut that is capable of forward and aft travel of over 3 ft in the streamwise direction. A main sting support attached to the strut can transverse laterally ±20 in. and can provide a yaw capability of ±12 deg. Forward of the main sting support is the angle-of-attack mechanism that provides pitch motion from −15 to +30 deg. A roll mechanism can be installed ahead of the pitch mechanism to provide continuous roll motion over a 310-deg range.

Instrumentation and Data Reduction

Three aerodynamic forces and three aerodynamic moments were measured using standard Langley six-component strain-gauge balances. Five different $\frac{9}{16}$-in.-diam, water-cooled balances were used for testing in the hypersonic facilities to accommodate different loadings and to perform balance to balance comparisons. Wind-off balance readings were monitored before and after each run, and balance components were monitored during the tunnel run for drift caused by thermal gradients across the balance gauges. Balance data were acquired in a pitch/pause manner (as opposed to continuous sweep) in all facilities, with a pause typically lasting 3–5 s at a given attitude. Data were averaged over 1 s with an acquisition rate of 20 samples/s. The model attitude was set at the strut head by a calibrated encoder and corrected postrun for sting deflections under load. Regardless of support system or orientation, the model was maintained within a uniform test core ($<\pm 1\%$ pitot pressure variation across the test core) as defined by tunnel flowfield surveys.

A conservative estimate of uncertainty applied to the data is a balance precision error of $\pm 0.5\%$ of the full-scale balance loads. Balance accuracies (in the absence of temperature variations), determined by multiple loadings conducted in LaRC calibration laboratories, are generally much smaller (from ± 0.1 to $\pm 0.3\%$ of the full-scale load). It has been an accepted practice in the AFC (based on recommendations from local balance manufacturers as well as a long history of force and moment testing in the AFC) to use an uncertainty of $\pm 0.5\%$ of full-scale loads to account for high-temperature effects because balances are not compensated for temperature variations. Diagnostic runs with the model held at a constant angle of attack for the entire duration of a blowdown run were periodically performed throughout the test to monitor balance performance with temperature. A listing of balances used in this study and the uncertainties for representative flow conditions are shown in Tables 3 and 4.

For aerodynamic testing, cavity pressure and limited base pressure measurements were obtained with external tubing and offboard transducers (as discussed subsequently). The level and variation of base pressure measurements revealed that base pressure corrections were negligible for the conditions of this study.

Test Parameters

A summary of the test matrices for all of the hypersonic aerodynamic data, including information about model parametrics and support structure for tests in each facility, is presented in Table 5. The model angle of attack ranged from -4 to 50 deg with the model mounted on a straight sting as well as on a blade strut for selected portions of this angle of attack range. Deflectable control surfaces included body flaps (from -15 to $+30$ deg), elevons (from -10 to $+30$ deg), and rudders (no deflections tested hypersonically), with increments shown in Table 5. The majority of runs were made with a single control surface, that is, only the right body flap or right elevon, deflected to obtain both a symmetric control surface increment (the assumption of symmetric superposition was spot checked)

Table 3 Balance matrix

Balance	Mach 6 air	Mach 10 air	Mach 6 CF_4	Mach 20 He	UPWT-leg II
SS08	S/B[a]	S/B	S	——	S
SS17A	S/B	S/B	B	——	——
2045	S	——	S	——	——
2047	——	——	——	S	——
2048	S	——	——	——	——

[a]S is straight sting mount and B is 45-deg blade mount.

Table 4 Balance uncertainties[a] for ±0.5% full scale

Facility	q_∞	C_N	C_A	C_m	C_l	C_n	C_Y
20-Inch Mach 6 air	2	0.022	0.0044	0.0029	0.0014	0.0007	0.0044
31-Inch Mach 10 air	2.2	0.020	0.0040	0.0026	0.0013	0.0007	0.0040
20-Inch Mach 6 CF_4	0.9	0.025	0.0049	0.0065	0.0016	0.0016	0.0049
22-Inch Mach 20 He	1.7	0.010	0.0018	0.0020	0.0007	0.0007	0.0021
UPWT-leg II	1.5	0.029	0.0059	0.0039	0.0019	0.0010	0.0059

[a]Based on highest full-scale balance loads when data obtained from multiple balances.

Table 5 Summary of test parametrics

Configuration	20-Inch Mach 6, air	31-Inch Mach 10, air[b]	20-Inch Mach 6, CF_4	22-Inch Mach 20, He[c]	UPWT-leg II air
Baseline	S/B[a]	S/B	S/B	S	S
−15-deg body flap	S/B	B	B	——	——
+10-deg body flap	S/B	B	B	S	——
+20-deg body flap	S/B	B	B	S	——
+30-deg body flap	S/B	B	S/B	S	——
−30-deg elevon	S/B	B	B	S	——
−20-deg elevon	S/B	B	B	S	——
−10-deg elevon	S/B	B	——	S	——
+10-deg elevon	S/B	B	——	S	——
+20-deg elevon	S/B	B	——	S	——
+30-deg elevon	S/B	B	——	S	——
Baseline fins	S/B	B	B	S	——
Baseline flaps	S/B	B	B	S	——
Baseline fins, flaps	S/B	B	B	S	——
Baseline fins, flaps, engine	S/B	B	——	——	——

[a]S is straight sting mount and B is 45-deg blade mount.
[b]Unable to get high-angle-of-attack range with sting mount.
[c]All runs in Mach 20 helium without vertical tails.

and an asymmetric aileron increment. Because of time and resource constraints, data were not obtained for coupled control surface deflections. To understand the individual contributions of the various aerodynamic surfaces to vehicle trim characteristics, a configuration buildup study was conducted to complement the existing hypersonic aerodynamic database. Configurations compared were the baseline vehicle, the baseline without canted fins, the baseline without body flaps, the baseline without fins and flaps (basic body with aerospike engine nozzle and vertical tails), and the baseline without fins, flaps, and engine nozzle.

Computational Methods

To complement the experimental database and to provide data at flight conditions, CFD calculations were performed for selected configurations over a range of angles of attack, Reynolds numbers, and Mach numbers in multiple test gases. Two finite volume, Navier–Stokes solvers, LAURA and GASP, and an inviscid Euler code, FELISA, were used to obtain aerodynamic data. Computational results at Mach 6 and 10 will be presented with the experimental data in subsequent sections. A thorough discussion of CFD codes, models, and data are presented in Ref. 8.

Results and Discussion

Preface

Over a 12-month period, more than 800 wind tunnel runs were completed in five LaRC facilities to provide benchmark aerodynamic data in the hypersonic regime for establishment of the X-33 flight database. A subset of these data, in concert with complementary computational aerodynamic data, is presented and discussed herein to meet the research objectives earlier outlined. A more detailed presentation of the research effort in support of the X-33 hypersonic aerodynamic database can be found in Ref. 9.

Figure 4 shows the aerodynamic coordinate system used for data measurement and analysis, including the sign convention for all force and moments and control deflections. Longitudinal aerodynamic data are presented in coefficient form for both body axes, C_N, C_A, and C_m, and stability axes, C_L, C_D, and L/D. Lateral-directional data are presented via the stability derivatives $C_{l\beta}$ and $C_{n\beta}$. All pitching moment data are referenced to a longitudinal c.g. located at 66% of vehicle reference length, defined as the distance from the nose to the engine ramp edge on the vehicle centerline. The lateral reference length is defined as the spanwise distance between canted fin root locations. The lateral c.g. location is on the body centerline, and the vertical c.g. location is at the zero waterline reference.

In the sections to follow, the aerodynamic data obtained in air, helium, and CF_4 test gases over a Mach number range of 4.63–20 are presented for the baseline X-33 configuration. [Data were obtained over a range of Reynolds number Re_∞ from 0.5×10^6 to 8×10^6/ft, and Reynolds number effects on aerodynamic characteristics were

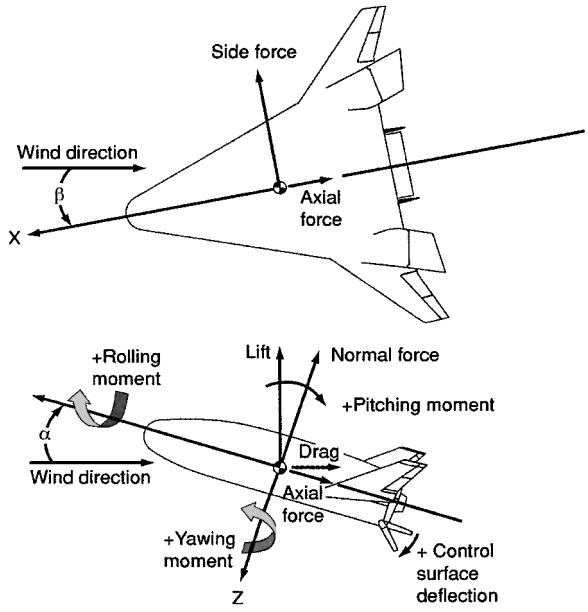

Fig. 4 Aerodynamic coordinate system.

shown to be negligible[6] and, therefore, will not be presented. Note that companion aeroheating tests showed that these values of Reynolds number Re_∞ correspond to laminar conditions on the vehicle fuselage; thus, care must be expressed in applying these finding to turbulent flow conditions, which are expected to occur on the flight vehicle at Mach 6 (Ref. 10)]. The effects of Mach number and specific heat ratio are presented for baseline longitudinal aerodynamic characteristics. Following results on the baseline configuration, body flap and elevon effectiveness are presented, discussing Mach number and specific heat ratio effects on longitudinal control authority. Companion inviscid and viscous CFD data are also presented in conjunction with aforementioned data sets. To enhance understanding of X-33 hypersonic aerodynamic characteristics, longitudinal aerodynamic results from configuration buildup studies will also be discussed.

Baseline Configuration

Mach Number Effects

The longitudinal characteristics of the baseline X-33 configuration are shown in Figs. 5a–5f, with both experimental and computational results for Mach 6 and 10 air plotted vs vehicle angle of attack. Lower angle-of-attack ($\alpha < 25$ deg) data were obtained with the model supported on a straight sting; higher angle-of-attack ($\alpha > 25$ deg) data were obtained with the model supported on a blade sting. The experimental results presented in Fig. 5 are curve fits to the data set. (Except where noted, experimental data in this report are represented by curve fits across the angle-of-attack range and computational data are presented as discrete data at specific angles of attack.)

Lift coefficient data for Mach 6 and 10 in air at a Reynolds number Re_∞ of 2×10^6/ft are presented in Fig. 5d. The experimental and computational data exhibit nearly linear behavior between $\alpha = 10$ and 36 deg, with a lift curve slope $C_{L\alpha}$ of approximately 0.024 and nonlinear behavior for angles of attack greater than 40 deg. C_{L0} values are identical for Mach 6 and 10 and are negative due to negative fin incidence. At angles of attack greater than 5 deg, the experimental and computational C_L values for Mach 6 are somewhat higher than for Mach 10, which is a previously observed trend with Mach number for other lifting reentry configurations.[11,12] The maximum deviation between experimental data sets occurs around $\alpha = 20$ deg, which corresponds to the maximum differences in both the normal and axial forces on the configuration (Figs. 5a and 5b). Computational values of C_N and C_A across the angle-of-attack range generally show good agreement (within balance accuracy bounds) in trend and magnitude with experimental data, with the exception of LAURA axial-force calculations, which predicts slightly lower levels at Mach 6 than trends predicted with GASP solutions. Experimental

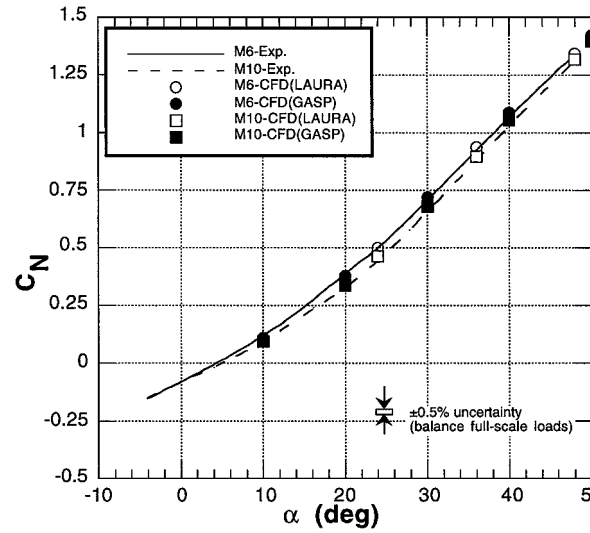

Fig. 5a Comparison of measured and predicted normal-force coefficient for Mach 6 and 10 ($Re = 2 \times 10^6$/ft).

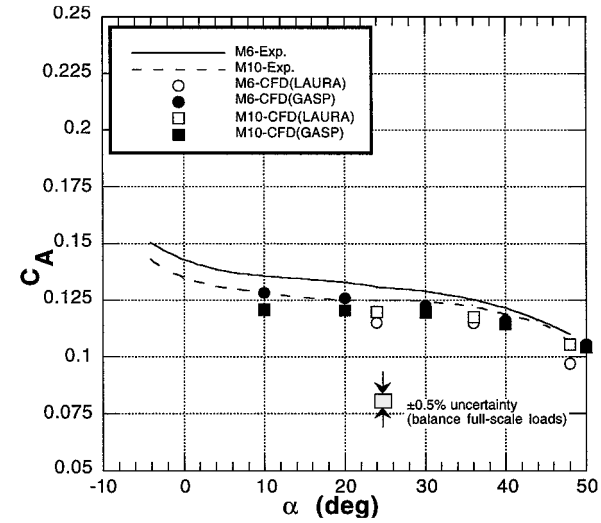

Fig. 5b Comparison of measured and predicted axial-force coefficient for Mach 6 and 10 ($Re = 2 \times 10^6$/ft).

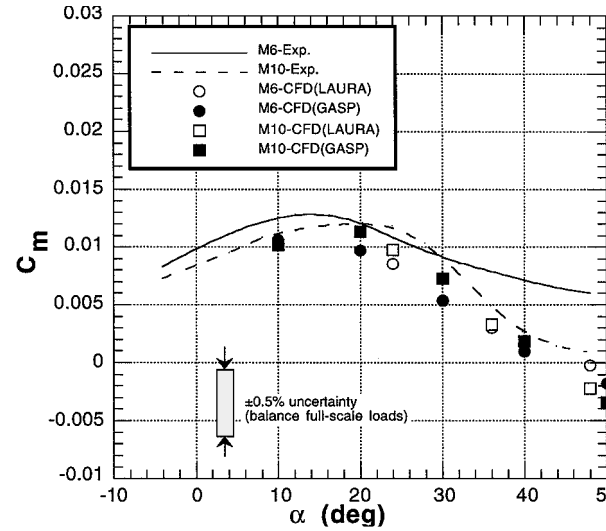

Fig. 5c Comparison of measured and predicted pitching-moment coefficient for Mach 6 and 10 ($Re = 2 \times 10^6$/ft).

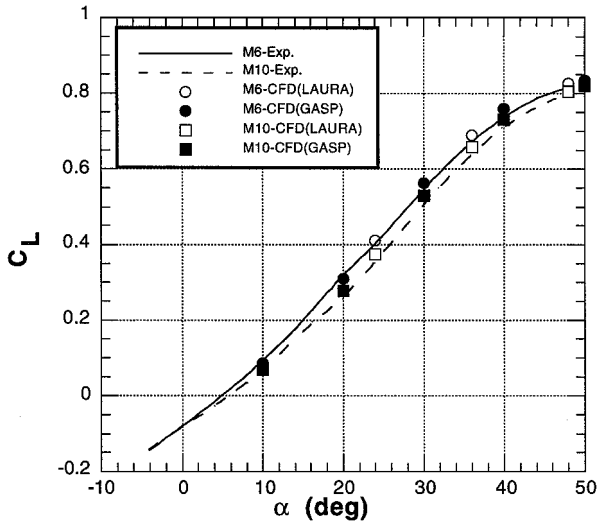

Fig. 5d Comparison of measured and predicted lift coefficient for Mach 6 and 10 ($Re = 2 \times 10^6$/ft).

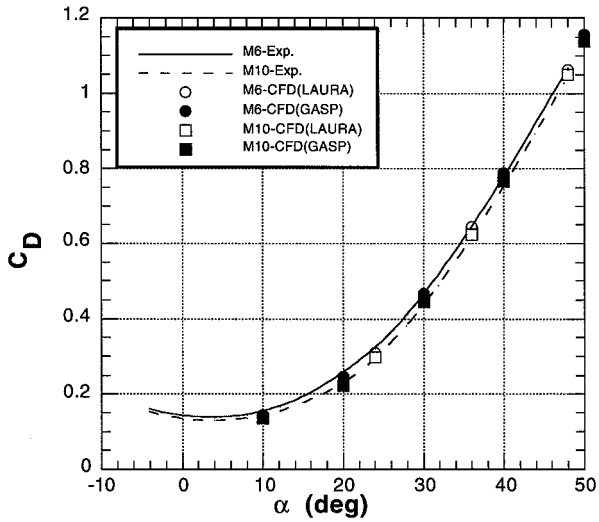

Fig. 5e Comparison of measured and predicted drag coefficient for Mach 6 and 10 ($Re = 2 \times 10^6$/ft).

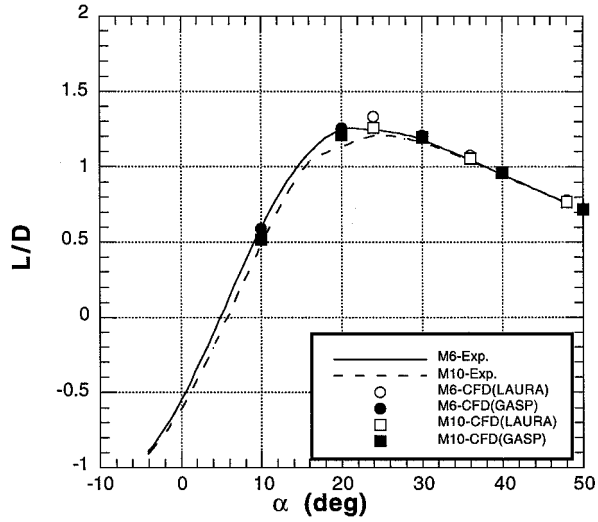

Fig. 5f Comparison of measured and predicted lift-to-drag ratio for Mach 6 and 10 ($Re = 2 \times 10^6$/ft).

data sets for C_D and L/D (Figs. 5e and 5f) exhibit similar Mach number effects with maximum deltas between Mach 6 and 10 occurring around $\alpha = 20$ deg. Figure 5f shows the hypersonic $(L/D)_{\max}$ to be approximately 1.2 between 20- and 30-deg angle of attack. Overall, compressibility effects are small for longitudinal force data.

Pitching-moment characteristics are shown in Fig. 5c. Recall that all pitching-moment data are referenced to a c.g. location at 66% of vehicle length. For this c.g. location, the configuration is longitudinally unstable (positive $C_{m\alpha}$) for $\alpha < 10$ deg and longitudinally stable (negative $C_{m\alpha}$) for $\alpha > 24$ deg for both Mach 6 and 10. Experimental data show the vehicle to be more stable at Mach 10 than Mach 6; computational data show the same trend but show this difference in stability level to be noticeably smaller. The greatest differences in C_m values between Mach 6 and 10 experimental data and between experimental and computational data occur at the higher angles of attack. The difference between Mach 6 and 10 data at $\alpha = 48$ deg is approximately 0.005; the difference between experiment and CFD at this same angle of attack is 0.006 and 0.003 for Mach 6 and 10, respectively. These differences raised questions about possible differences between computational and experimental models. For example, errors introduced into the CFD calculations due to inaccurate modeling of the base region were initially unknown. An additional Mach 6 CFD calculation with a full laminar wake $\alpha = 36$ deg was compared to calculations with the extended surface model discussed previously, and this comparison showed little effect of the base flow on pitching moment.[10] The measured pitching-moment curves exhibit a crossover in the midalpha range (20–30 deg) as do the CFD predictions (further discussed subsequently), although at a higher angle of attack. A similar trend has also been observed experimentally for the X-38 lifting-body configuration.[13] In an effort to understand the flow phenomena contributing to the trends in pitching moment as a function of angle of attack, a configuration buildup study was conducted, and these results will be discussed at the end of this section.

It is instructive to further examine the pitching moment database in light of data repeatability and control authority to understand the nature and significance of the observed differences at Mach 6 and 10. Figure 6a shows pitching-moment data points generated for the baseline configuration for Mach 6 and 10 with both sting and blade-mount supports. These data represent numerous repeat runs and results with different strain-gauge balances. Compared with the pitching-moment plot of Fig. 5c, a highly expanded scale is used in Fig. 6a to allow delineation of individual data points. Two shaded gray bands are drawn to show the extent of C_m variation for both Mach numbers. Note that, for all data presented, the range of C_m values for a given angle of attack are within the $\pm 0.5\%$ of full-scale balance load accuracy already discussed. The variation in the Mach 6 data set is less than $\pm 0.25\%$ of full-scale balance load accuracy throughout the angle-of-attack range, and model support appears to have no significant influence on pitching moment trends for $\alpha > 20$ deg. The Mach 10 data are characterized by larger scatter throughout the angle-of-attack range and noticeable differences between the sting and blade mounts; however, these data still remain within the $\pm 0.5\%$ balance load accuracy band. The total temperature in the Mach 10 facility is approximately twice that of the Mach 6 facility, and although great care was taken to monitor and to attempt to minimize temperature effects, thermal gradients across the model and balance led to higher levels of uncertainty for measurements at Mach 10. The differences between the sting and blade data observed at Mach 10 across the angle-of-attack range are relatively small. The data presented in Fig. 6a also represent runs with different balances in both upright and inverted orientations. Thus, the general pitching moment trends observed experimentally for Mach 6 and 10 were shown to be repeatable.

Figure 6b shows body flap control authority for Mach 6 relative to the baseline Mach 6 and 10 data sets presented in Fig. 6a. The observed differences on experimentally measured pitching moment data at Mach 6 and 10 correspond to only 2–3 deg of body flap deflection. Given a 66% c.g. location, this increment is a small percentage of the total flap deflection available to control the vehicle at hypersonic conditions. Further discussion of longitudinal control authority can be found in the section to follow.

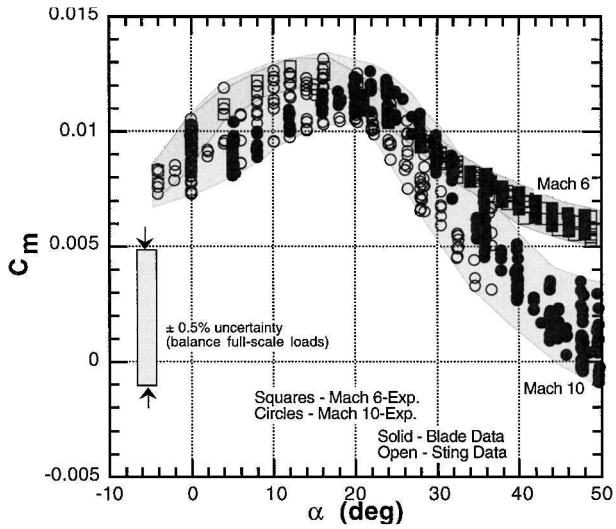

Fig. 6a Repeatability of Mach 6 and 10 experimental data (Re = 2×10^6/ft).

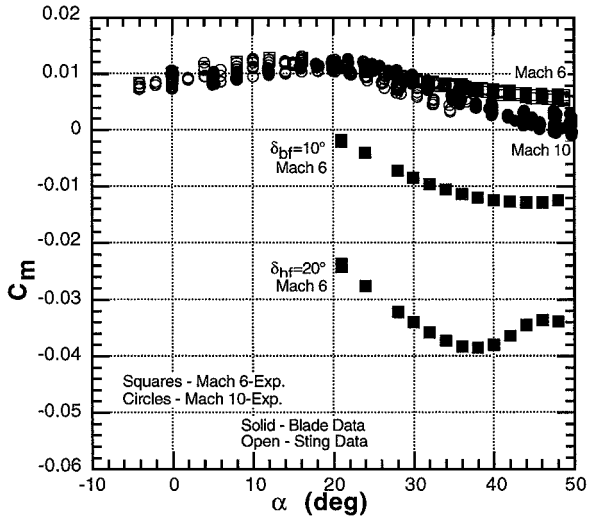

Fig. 6b Measured body flap control authority at Mach 6 relative to repeatability of Mach 6 and 10 experimental data ($Re = 2 \times 10^6$/ft).

A great deal of testing was performed in the NASA Marshall Space Flight Center (MSFC) 14-Inch by 14-Inch trisonic facility to populate the transonic/supersonic database for the X-33,[5] and these data will naturally be merged with the hypersonic database generated at LaRC. (Additional tests are also planned sometime in 2001 in Lockheed Martin's Vought Facility to obtain higher-Reynolds-number data in these flight regimes.) However, the data generated at MSFC were not at sufficiently high angles of attack for comparison with the present hypersonic database. Therefore, a brief entry of the baseline configuration in LaRC's UPWT was performed to provide additional high supersonic data up to $\alpha = 40$ deg with the LaRC 0.007-scale model and a hypersonic force and moment balance (eliminating model/balance/support variation) to complement the hypersonic database. Figures 7a–7c show the longitudinal aerodynamic characteristics (body axis only) of the X-33 configuration obtained at Mach 4.63 plotted with the Mach 6 and 10 data. Both normal and axial force coefficients show a systematic trend with Mach number. There is excellent agreement between experiment and both viscous and inviscid prediction of C_N at $M = 4.63$. Inviscid predictions of C_A fall below the measured values as expected, and predicted C_A from the LAURA code falls below the measured value as was also observed at Mach 6 and 10 (Fig. 5b). The pitching-moment data obtained from these UPWT tests, shown in Fig. 7c, exhibit similar trends to those observed for Mach 6. The pitching-moment curves exhibit a crossover with the Mach 10 data at $\alpha = 36$ deg, compared to the Mach 6 crossover with the Mach 10 data at $\alpha = 30$ deg. Supporting inviscid and viscous CFD calculations at Mach 4.63 are in excellent agreement with experimental pitching-moment data from the UPWT. Figure 7d, adapted from Ref. 8, shows a set of M–α parametric calculations run for the X-33 configuration using the GASP code. Although on a smaller scale, the computational data clearly show a crossover trend with Mach number. The experimental data for $M = 4.63$, 6, and 10, for a given Reynolds number Re_∞ and γ_∞, coupled with the GASP parametric calculations for the same Mach number range, reveal that pitching moment for the LMSW X-33 baseline configuration is dependent on Mach number. For angles of attack up to 48 deg, the baseline configuration did not trim for any of the Mach numbers tested, but ample control authority (to be discussed subsequently) exists to achieve a trimmed condition for any angle of attack.

Figures 8a and 8b present the lateral-directional stability characteristics $C_{l\beta}$ and $C_{n\beta}$ for the X-33 vehicle for Mach 6 and 10. The vehicle is stable in roll (negative values of $C_{l\beta}$) for all but the lowest angles of attack tested ($\alpha < 4$ deg) for both Mach 6 and 10. The vehicle demonstrates positive dihedral effect, and roll stability increases nearly linearly as the angle of attack increases and the wing dihedral becomes more effective. $C_{n\beta}$ is nearly a constant negative value across the angle-of-attack range for Mach 6 and 10, indicating that the vehicle is directionally unstable. The small twin vertical tails on the aft upper surface do little to affect yaw stability, especially at typical hypersonic reentry attitudes, that is, high angle of attack, when they are shielded from the incoming flow. This lack of directional control is a common trait of winged or lifting-body entry vehicles and generally necessitates the use of reaction control jets. For this reason, no rudder deflections were examined at Mach 6 and 10, and no further discussion of lateral-directional characteristics will be presented.

Specific Heat Ratio Effects

Past experience with the space Shuttle Orbiter has shown the importance of real-gas effects on overall vehicle aerodynamics and control authority. During the high-Mach-number, high-altitude portion of the first entry of the orbiter (STS-1), the vehicle exhibited a nose-up pitching moment relative to preflight prediction of approximately $\Delta C_m = 0.03$. This trim anomaly has now been attributed to lower than expected pressures on the aft windward surface as a result of real-gas effects, and the pitch increment experienced in flight was accurately simulated by testing a model of the orbiter in the 20-Inch Mach 6 CF_4 Tunnel.[12] The X-33 program seeks to use preflight data from the CF_4 tunnel to determine whether the current X-33 configuration has a potential for significant real-gas effects as observed on the Space Shuttle Orbiter.

Within the AFC facilities, testing the same model in the Mach 6 air and CF_4 tunnels allows isolation of the effects of shock density ratio (or postshock specific heat ratio, γ_2) because both freestream Mach number and unit Reynolds number can be matched. Schlieren photographs (Figs. 9a and 9b) of the 0.007-scale X-33 model in air and CF_4 clearly show the decrease in shock standoff distance due to the increased shock density ratio in CF_4.

To examine the full range of γ_2 values available in the LaRC hypersonic facilities, data from Mach 10 air and Mach 20 helium are included with the Mach 6 air and CF_4 comparisons to be discussed subsequently. (These facilities do not permit testing at the same Mach number and Reynolds number, but based on the preceding two sections, the effects of these parameters are known and generally small.) The values of postshock specific heat ratio for the AFC facilities are as follows: $\gamma_2 = 1.15$ for Mach 6 CF_4, $\gamma_2 = 1.35$ for Mach 10 air, $\gamma_2 = 1.4$ for Mach 6 air, and $\gamma_2 = 1.67$ for Mach 20 helium. Both Mach 6 CF_4 and Mach 10 air exhibit lower γ_2 values than γ_∞ due to vibrational excitation associated with higher temperatures. Figures 10a–10c present normal-force, axial-force, and pitching-moment coefficients obtained in CF_4 and helium as compared with the already discussed Mach 6 and 10 air data to examine the effects of shock density ratio (or γ_2) on longitudinal aerodynamics. There is little effect of γ_2 on C_N (Fig. 10a), with the CF_4 and helium data results being bounded by the Mach 6 and 10 data discussed earlier for compressibility effects. The axial-force coefficient variation from the four facilities is shown in Fig. 10b. The observed

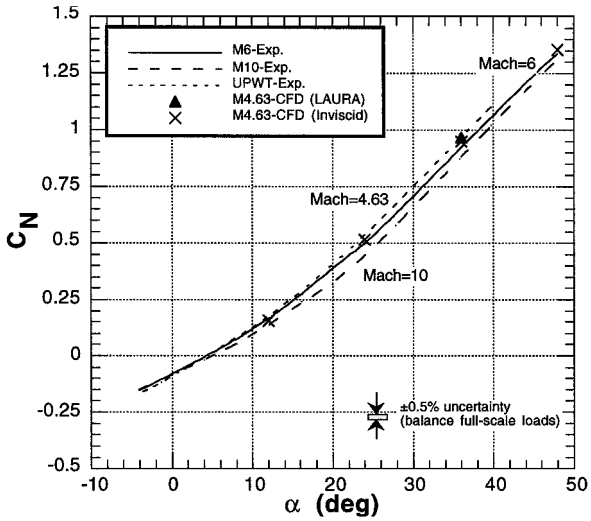

Fig. 7a Comparison of measured and predicted normal-force coefficient for Mach 4.63, 6, and 10 ($Re = 2 \times 10^6$/ft).

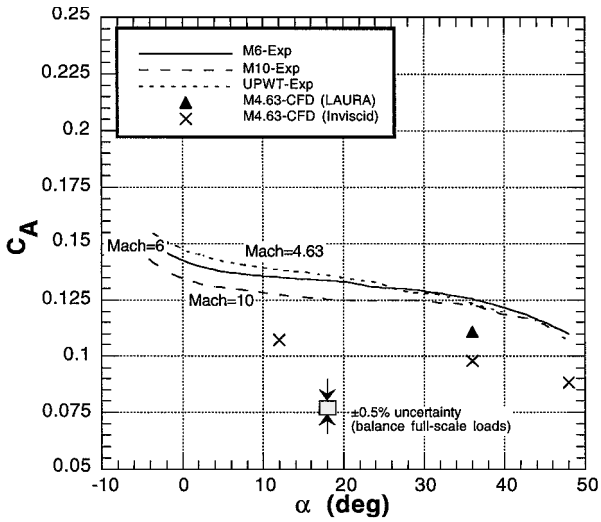

Fig. 7b Comparison of measured and predicted axial-force coefficient for Mach 4.63, 6, and 10 ($Re = 2 \times 10^6$/ft).

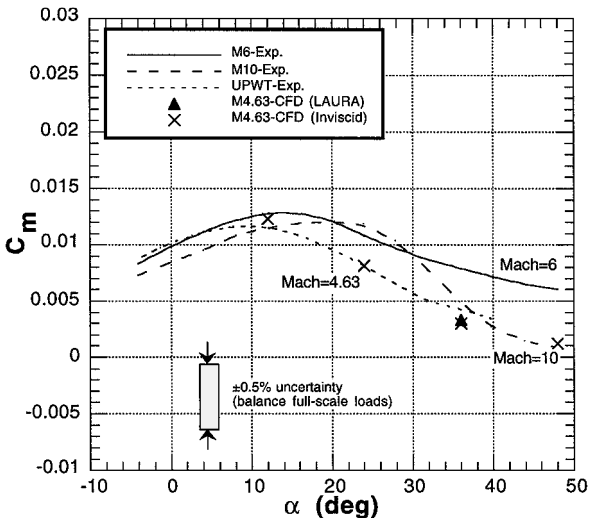

Fig. 7c Comparison of measured and predicted pitching-moment coefficient for Mach 4.63, 6, and 10 ($Re = 2 \times 10^6$/ft).

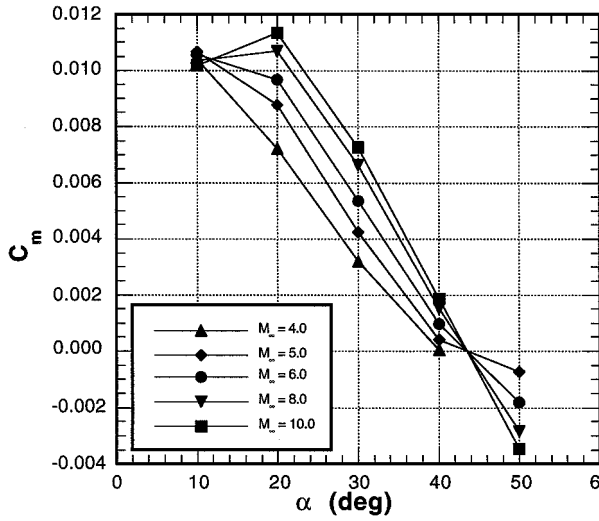

Fig. 7d Comparison of measured and predicted pitching-moment coefficient for Mach 4.63, 6, and 10 ($Re = 2 \times 10^6$/ft) (from Ref. 8).

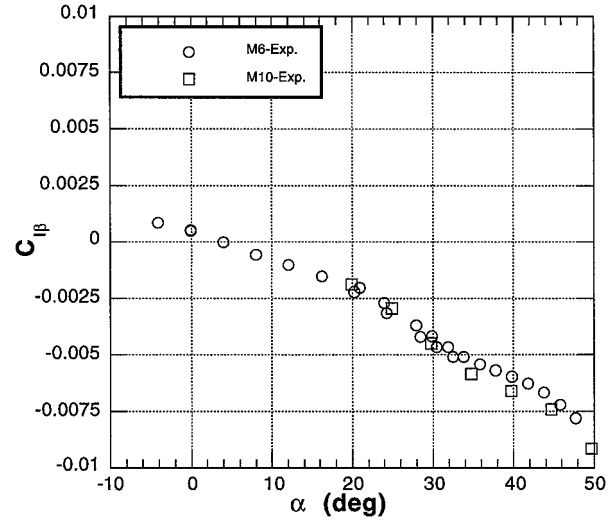

Fig. 8a Dihedral effect for Mach 6 and 10 experimental data ($Re = 2 \times 10^6$/ft).

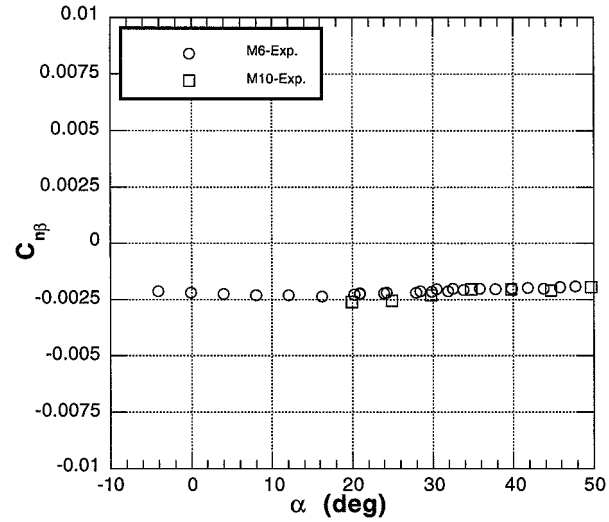

Fig. 8b Directional stability for Mach 6 and 10 experimental data ($Re = 2 \times 10^6$/ft).

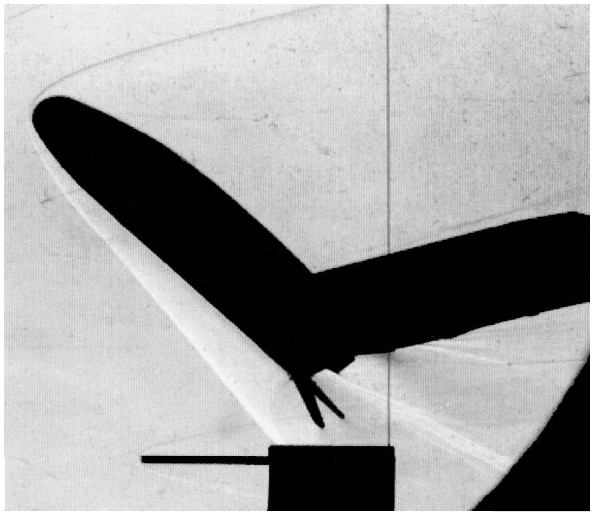

Fig. 9a Schlieren photograph at α = 48 deg in 20-Inch Mach 6 tunnel ($Re = 2 \times 10^6$/ft).

Fig. 9b Schlieren photograph at α = 48 deg in 20-Inch Mach 6 CF_4 Tunnel ($Re = 0.5 \times 10^6$/ft).

variation in C_A with angle of attack is the same qualitatively for all four test conditions. However, the pitching-moment coefficient, plotted in Fig. 10c, shows a significant sensitivity to γ_2 with a clear change in stability and trim characteristics at the higher angles of attack. For $\alpha > 35$ deg, the C_m data in helium (which, in terms of ρ_2/ρ_∞, simulates Mach 3.2 in air) become unstable with more nose-up pitching moment than the air data. The CF_4 data, which simulate Mach 13–18 in flight, show the opposite trend, with the vehicle becoming more longitudinally stable and more nose-down as compared to both the Mach 6 and 10 data sets. The pitching-moment values and the stability levels have a consistent trend with decreasing γ_2 or increasing ρ_2/ρ_∞. Inviscid calculations[14] for Mach 6 and 10 air, Mach 6 CF_4, and Mach 20 helium (Fig. 10d) support the measured trends shown in Fig. 10c. These calculations (shown in Ref. 8 to be in very good agreement with viscous results for air and CF_4 pitching-moment predictions) clearly show the unstable pitch-up in helium and the increase in stability and pitch-down in CF_4 at high angles of attack. The primary effect of a real gas on aerodynamic characteristics is to lower specific heat ratio within the shock layer, γ_2, resulting in a greater degree of flow compression or expansion relative to perfect-gas air where γ_2 is higher. The Space Shuttle Orbiter experienced lower pressures on its aft windward expansion surface, resulting in a significant nose-up pitch increment. A model of the X-38 vehicle tested in the CF_4 tunnel also showed a pitch-up, although much smaller in magnitude compared to the orbiter, due to the aft boattail of the X-38.[13] The X-33's nose-down

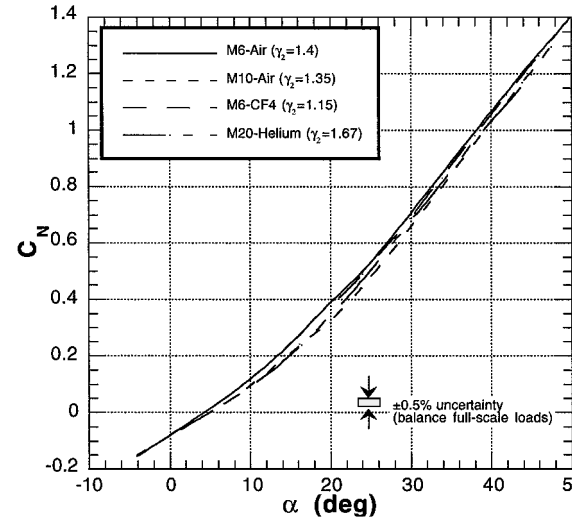

Fig. 10a Effect of shock density ratio on measured normal-force coefficient.

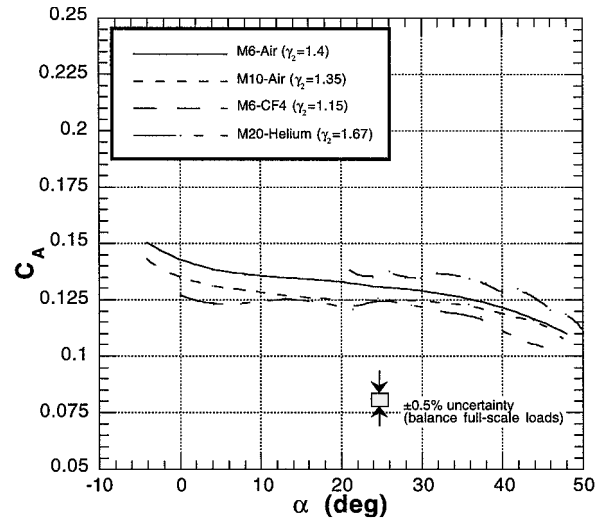

Fig. 10b Effect of shock density ratio on measured axial-force coefficient.

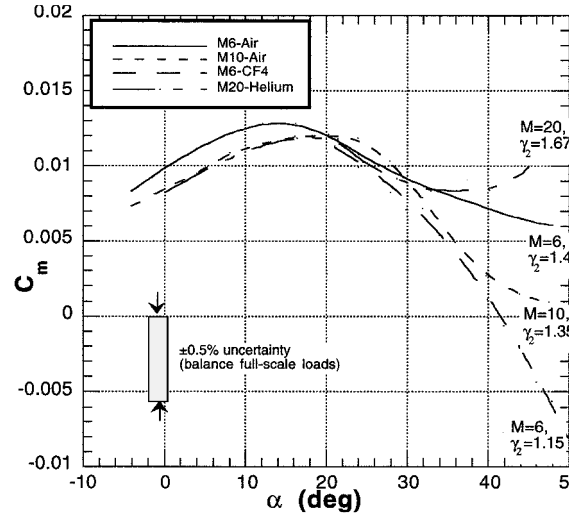

Fig. 10c Effect of shock density ratio on measured pitching-moment coefficient.

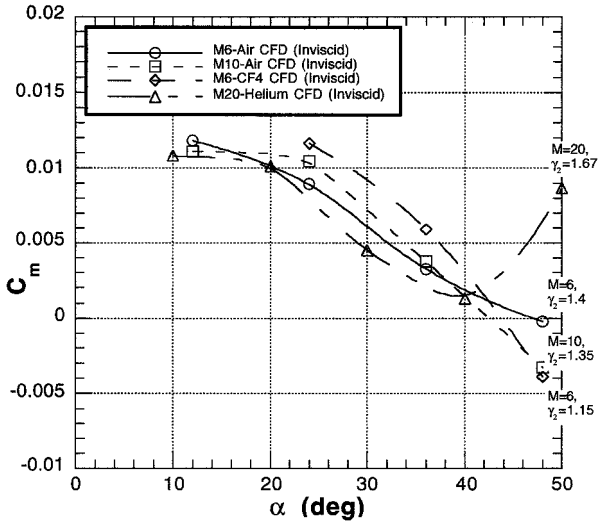

Fig. 10d Effect of Mach number and shock density ratio on predicted pitching-moment coefficient.

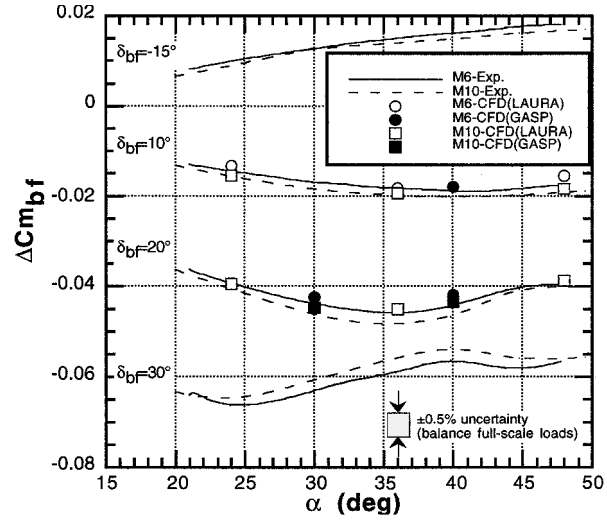

Fig. 11a Comparison of measured and predicted body flap control authority for Mach 6 and 10 ($Re = 2 \times 10^6$/ft).

pitch increment observed in the CF_4 data indicates a distinct difference between the X-33 configuration and these other lifting reentry configurations. Aft windward compression surfaces and/or leeside flow expansion around the vehicle's nose region are likely to be the primary contributors to real-gas increments on pitching moment for the X-33 configuration.

In viewing these data, there are two additional points to consider: 1) Whereas the effects of γ_2 variation, that is, simulated real-gas effect, on pitching moment are shown to be more significant than Mach number effects, they are still small in comparison (and opposite in sign) to those previously observed for the shuttle. More will be said regarding the magnitude of these γ_2 effects in the section discussing longitudinal control authority. 2) With a maximum flight Mach number of only about 10, significant real-gas phenomena will not occur for the X-33's suborbital flight. CF_4 data for the X-33 will be used to gauge the significance of real-gas effects for an X-33 derived RLV, which will fly a higher-Mach-number reentry trajectory, and, therefore, are a valuable part of the X-33 hypersonic database.

Longitudinal Control Authority

Mach Number Effects

The body flap effectiveness, ΔC_m, for four flap deflection angles at vehicle angles of attack from 20 to 50 deg for Mach 6 and 10 in air is presented in Fig. 11a. Curve fits were applied to measured data for which only one of the two body flaps were deflected (the other remained at zero deflection). The results presented in Fig. 11a, however, represent simultaneous deflection of both body flaps and have been constructed by doubling the ΔC_m measured from a single body flap deflection. This superposition assumption was checked against actual symmetric deflections, that is, both body flaps deflected the same amount, and the results were indistinguishable. Cross talk between the flaps is not expected because the local flow in the aft region of the fuselage windward surface is supersonic, streamline patterns indicate outflow at the higher angles of attack, and the flaps are not in proximity to each other. For both Mach 6 and 10 experimental data, the increment in C_m due to deflecting the body flaps up ($\delta_{bf} = -15$ deg) is positive and increases with angle of attack, appearing to asymptote to a constant value at the highest angles of attack. The remaining sets of data represent down-flap deflections of 10, 20, and 30 deg. A 10-deg flap deflection provides a negative pitch increment for Mach 6 and 10, the magnitude of which smoothly increases with angle of attack to a nearly constant value of approximately $\Delta C_{m\,bf} = -0.02$ for both Mach numbers. Recalling the baseline pitching moment curves in Fig. 5c, one can see that a 10-deg flap deflection produces more than twice the control authority needed to trim the vehicle at both Mach 6 and 10.

As the flap is further deflected downward to 20 and 30 deg, flap effectiveness becomes nonlinear with angle of attack. To explain this behavior, experimental heating data, surface streamline

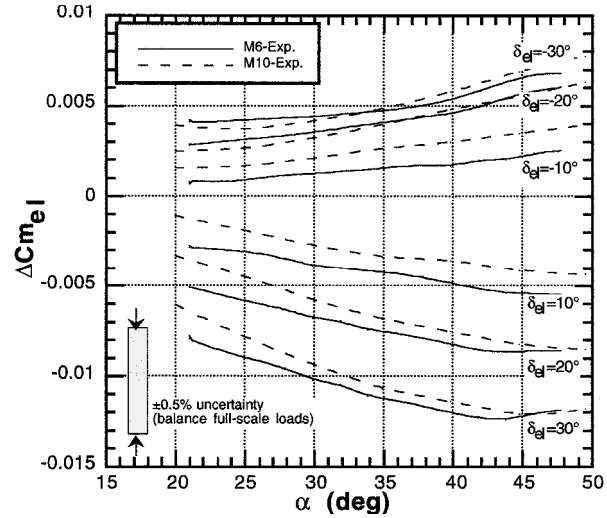

Fig. 11b Measured elevon control authority for Mach 6 and 10 ($Re = 2 \times 10^6$/ft).

and flowfield visualization techniques, and computational solutions were used to complement the aerodynamic data. Mach 6 aeroheating results[3] showed a complex heating pattern on the windward surface of the 20-deg flap and a well-defined disturbance in accompanying oil-flow visualizations at $\alpha = 40$ deg. Schlieren photography at the same conditions clearly showed an interaction between the vehicle's windward bow shock and the flap shock. Viscous computations[4] revealed that this disturbance on the flap is due to the impingement of an expansion fan resulting from the bow shock/flap shock interaction. These computations also reveal the resulting decrease in surface pressures on the flap downstream of the impingement, which appears to be the cause of the nonlinear characteristics for larger flap deflection angles. That the surface pressure distribution on the flaps is influenced by the relative location of the bow and flap shocks may explain why larger differences are observed between Mach 6 and 10 pitch increments with increasing flap deflection. These nonlinear effects on pitching-moment increments are predicted quite well by laminar CFD calculations for $\delta_{bf} = 20$ deg (Fig. 11a). For the 30-deg flap deflection, the decrease in control effectiveness due to this shock/shock interaction begins at a lower angle of attack and is likely due to the steeper flap shock associated with the larger flap deflection. The aforementioned aeroheating results showed this flow structure to be highly dependent on the state of the boundary layer ahead of the deflected flap, as expected. (A turbulent boundary layer upstream of the deflected flap was obtained in Ref. 15 by physically tripping the boundary layer.) Over the Reynolds number range tested

with the present 0.007-scale metal model, it is believed, based on companion aeroheating data, that all force and moment data, and therefore body flap increment data, were obtained for laminar conditions only. Comparison of laminar and turbulent heating results in Ref. 3 revealed that these disturbances on the deflected flap are much less severe for a turbulent boundary layer approaching the flap; however, determination of changes in flap effectiveness due to the presence of turbulent flow cannot be made from the current data set. For all flap deflections, compressibility effects are small (within balance accuracy bounds) on body flap pitching moment effectiveness.

The elevon effectiveness is shown in Fig. 11b and again is the result of superposition of a single deflected surface. For both Mach 6 and 10 conditions, the elevons produce smaller pitching-moment increments than the body flaps due, in large measure, to a smaller total surface area and a shorter distance to the configuration c.g. The C_m increments due to increases in elevon deflection exhibit less nonlinearity than the body flaps. Elevons at the highest negative deflection ($\delta_{el} = -30$ deg) show a reduced increment (ΔC_m per degree of deflection) across the angle-of-attack range than observed for the body flap deflections. The positive elevon deflections provide a more linear behavior with increasing deflection and increasing angle of attack. The slight decrease in effectiveness at the highest angles of attack at both Mach 6 and 10 for $\delta_{el} = 20$ and 30 deg may be due to the effects of a larger laminar separation at the hinge line. As observed for the body flap, there are no significant compressibility effects for elevon longitudinal control authority.

Specific Heat Ratio Effects

As discussed earlier, real-gas effects during the hypervelocity portion of the Space Shuttle Orbiter's reentry flight trajectory proved to be significant and were accurately predicted, postflight, using CF_4 data. Real-gas effects influenced the overall vehicle pitching-moment characteristics and control surface effectiveness, resulting in the body flap having to be deflected more than twice preflight predictions to trim the vehicle. Figure 12 shows the effect of helium ($\gamma_2 = 1.67$) and CF_4 ($\gamma_2 = 1.15$) simulations on body flap effectiveness for flap deflections of 10 and 20 deg. As a general trend, the measured values of $\Delta C_{m\,bf}$ in helium tends to underpredict flap effectiveness, particularly at higher angles of attack, as compared with results in air. Therefore, testing in the helium tunnel will provide a conservative estimate of nose-down control authority. The helium data show the same nonlinear trend with angle of attack as discussed earlier for the air results (Fig. 11a), and the decrease in flap effectiveness begins at lower angle of attack in helium. For both a 10- and 20-deg flap deflection, the CF_4 data show a more effective flap over the angle-of-attack range tested. Thus, the measured data presented in Fig. 12 show a consistent trend: increasing control authority with decreasing γ_2. These results indicate that, for this configuration, real-gas effects lead to increased control authority. A real-gas exhibits greater flow compression than an ideal gas, and this may result in higher pressures on the windward surface of the body flaps. However, this increase is small relative to overall flap control authority.

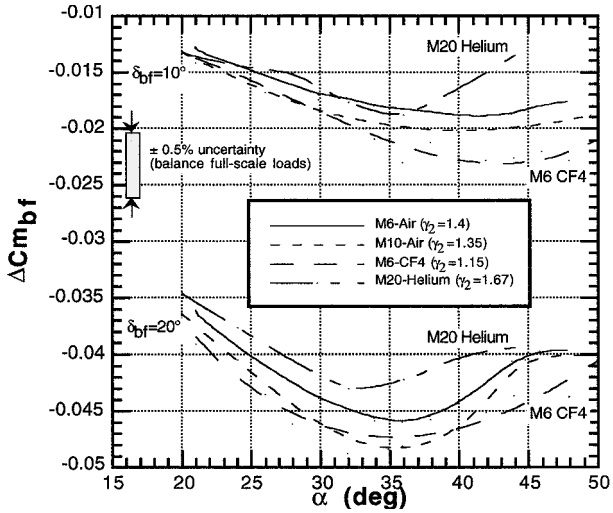

Fig. 12 Effect of shock density ratio on measured body flap control authority.

Configuration Buildup Studies

To understand the individual contribution of the various aerodynamic surfaces to vehicle longitudinal aerodynamic characteristics, an extensive configuration buildup study was conducted to complement the existing hypersonic aerodynamic database. Five configurations were tested: baseline, baseline without flaps, baseline without fins, baseline without flaps and fins, and baseline without flaps, fins, and engine nozzle. Configuration buildup studies were conducted in the 20-Inch Mach 6 Air Tunnel, the 31-Inch Mach 10 Air Tunnel, and the 20-Inch Mach 6 CF_4 Tunnel. The absence of the aerospike engine nozzle produced no measurable changes in the aerodynamic coefficients for any condition, and thus, no data are presented for this component. The primary driver for the configuration buildup study was to further examine compressibility effects on hypersonic pitching-moment characteristics of the X-33 configuration. It was hoped that comparison of buildup data at Mach 6 and 10 would provide additional insight into the pitching-moment crossover trend by identifying individual component contributions.

Figures 13a–13c present the normal-force, axial-force, and pitching-moment coefficients for four buildup configurations over an angle-of-attack range of 20–50 deg for Mach 6 and 10 in air. Normal-force contributions (Fig. 13a) vary linearly with angle of attack and are proportional to the component surface area for all configurations tested. The baseline configuration has the highest values of C_N for both Mach 6 and 10, whereas the body alone (baseline without flaps and fins) yields the lowest C_N values, as expected due to reduced planform area. The small increments of normal force due to the fins and flaps clearly identify the body as the major contributor (approximately 80%) to vehicle normal force. At the highest angles of attack, the fins provide roughly twice the normal-force increment of the flaps, whereas at the lowest angles of attack, flap and fin normal force increments are approximately equal and a smaller percentage of the total C_N for the configuration. In general, the same compressibility increments occur for the four configurations at Mach 6 and 10.

Figure 13b presents the axial-force coefficient for the buildup configurations at Mach 6 and 10 in air. Note that the C_A scale on this plot is somewhat expanded from earlier plots to view trends more clearly. As observed for the normal-force coefficient, compressibility effects are generally similar for the four configurations. The easiest way to examine axial-force trends for the eight data sets in Fig. 13b is to notice that there are two distinct families of curves corresponding to configurations with and without canted fins. C_A values for the baseline without fins and flaps (body alone) and the baseline without fins increase with angle of attack up to approximately 40 deg and then begin to decrease slightly. The baseline and baseline without flaps have a maximum axial-force coefficient at the lowest angles of attack (approximately 20 deg) with a nonlinear decrease in C_A with increasing angle of attack. At lower angles of attack, higher axial-force contributions are observed for configurations with fins, due to pressure and skin-friction drag on the additional surfaces. However, this trend is reversed for angles of attack above 40 deg for both Mach 6 and 10. These data indicate that at higher angles of attack the axial force is less influenced by profile drag and more by the pressure field around the fins and at the aft end of the configuration. At higher angles of attack, the presence of the fins must reduce pressures on the base and around the fins in the axial direction.

Figure 13c shows the pitching-moment characteristics for the four buildup configurations at Mach 6 and 10 in air. Although the baseline configuration is slightly stable, the body alone (baseline without flaps and fins) is highly unstable. The presence of the flaps and fins, with nearly equal contributions, stabilize the vehicle over this angle-of-attack range. For both Mach 6 and 10, the flap and fin C_m increments add linearly to the body alone to produce the baseline curve, which indicate that interactions between these surface and the body

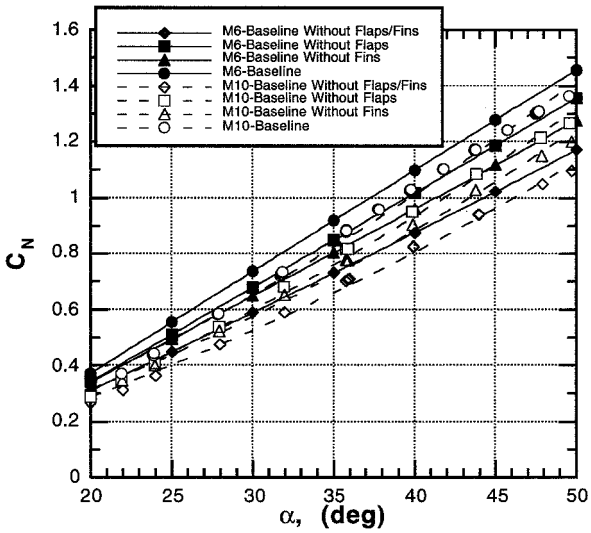

Fig. 13a Comparison of measured normal-force coefficient for Mach 6 and 10 for configuration buildup studies ($Re = 2 \times 10^6$/ft).

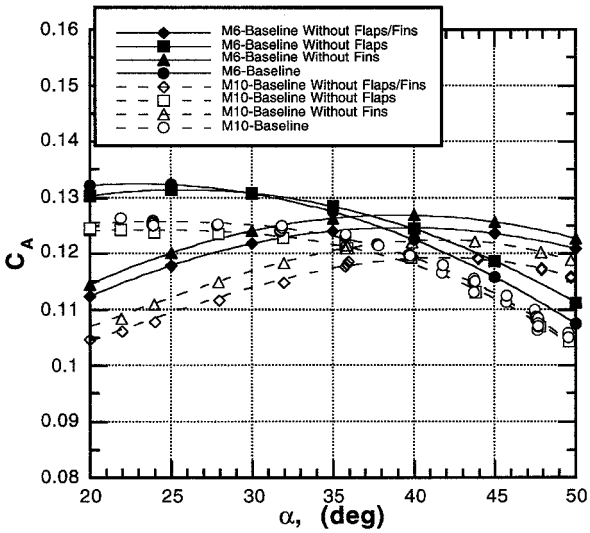

Fig. 13b Comparison of measured axial-force coefficient for Mach 6 and 10 for configuration buildup studies ($Re = 2 \times 10^6$/ft).

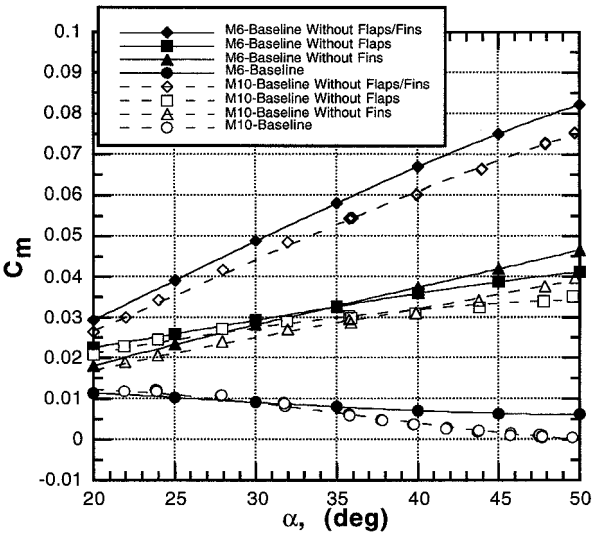

Fig. 13c Comparison of measured pitching-moment coefficient for Mach 6 and 10 for configuration buildup studies ($Re = 2 \times 10^6$/ft).

are not significant contributors to the pitching moment. Before these configuration buildup studies, it was thought that differences in the flowfields around the flaps, fins, or engine nozzle (possibly suggesting a freestream disturbance or partial tunnel blockage) could be the cause of the variation in pitching moment between Mach 6 and 10. Figure 13c clearly shows that the differences observed between Mach 6 and 10 baseline are also present for the body alone and are not caused by the flaps or fins at high angle of attack. Although the configuration buildup studies did not reveal the cause of Mach number effects on pitching-moment characteristics, it identified the body as the primary source. This information provides the foundation for possible future computational and experimental investigations of Mach number effects for this configuration.

Conclusions

NASA LaRC's Aerothermodynamics Branch has generated an extensive experimental and computational aerothermodynamic database in support of the development and flight of the LMSW X-33 lifting-body vehicle. This paper has described work performed by the authors to characterize the hypersonic aerodynamic characteristics of the X-33 flight-test vehicle (604B0002G configuration) currently being built by LMSW. In a 12-month period, over 800 wind-tunnel runs were completed in five supersonic/hypersonic facilities at LaRC to provide force and moment data for a range of flow simulation parameters. These results were complemented with computational aerodynamic data to enhance the understanding of experimentally observed aerodynamic trends.

Data at both Mach 6 and 10 show the baseline configuration achieves a maximum hypersonic L/D of approximately 1.2 between 20 and 30 deg angle of attack. With the c.g. location at 66% of vehicle reference length, the configuration was found to be longitudinally controllable with less than half of the total body flap deflection capability across the angle-of-attack range at both Mach 6 and 10. The vehicle also was shown to be longitudinally stable or neutrally stable for typical (greater than 20 deg) hypersonic flight attitudes. At Mach 6 and 10, the baseline configuration demonstrated positive dihedral effect (roll stability) but was directionally unstable. Effects of Mach number on longitudinal aerodynamics were shown to be repeatable but small relative to X-33 control authority. Configuration buildup studies identified the fuselage (as opposed to the canted fins or body flaps) as the primary source of compressibility effects on baseline pitching moment characteristics. Effects of specific heat ratio on vehicle pitching-moment characteristics were shown to be significant at higher angles of attack, but with a maximum flight Mach number of approximately 10, real-gas phenomena are not expected to occur for the X-33's suborbital flights.

The hypersonic aerodynamic data generated at LaRC have been used to populate the flight database for the X-33 vehicle. This database will be used to design the flight control laws and to optimize X-33 flight trajectories for demonstration of RLV technologies.

Acknowledgments

The authors wish to thank the many technicians and engineers at NASA Langley Research Center and the Aerodynamics Team at Lockheed-Martin Skunk Works without whose help this work would not have been possible.

References

[1]Reed, R. D., *Wingless Flight, The Lifting Body Story*, NASA SP-4220, Aug. 1997.

[2]Bekey, I., Powell, R., and Austin, R., "NASA Studies Access to Space," *Aerospace America*, Vol. 32, No. 5, 1994, pp. 38–43.

[3]Horvath, T. J., Berry, S. A., Hollis, B. R., Liechty, D. S., Hamilton, H. H., II, and Merski, N. R., "X-33 Experimental Aeroheating at Mach 6 Using Phosphor Thermography," *Journal of Spacecraft and Rockets*, Vol. 38, No. 5, 2001, pp. 634–645.

[4]Hollis, B. R., Horvath, T. J., Berry, S. A., Hamilton, H. H., II, Thompson, R. A., and Alter, S. J., "X-33 Computational Aeroheating Predictions and Comparisons with Experimental Data," *Journal of Spacecraft and Rockets*, Vol. 38, No. 5, 2001, pp. 658–669.

[5]Reasor, J. S., and Ramsey, J. F., "A Comparison of Wind Tunnel Data Taken For the X33 604B0002F/G Configuration," Lockheed Martin Skunk Works, Paper 604AERO5046, Palmdale, CA, June 1998.

[6]Micol, J. R., "Langley Aerothermodynamic Facilities Complex: Enhancements and Testing Capabilities," AIAA Paper 98-0147, Jan. 1998.

[7]Erickson, G. E., "Overview of Selected Measurement Techniques for Aerodynamic Testing in the NASA Langley Unitary Plan Wind Tunnel," AIAA Paper 2000-2396, June 2000.

[8]Hollis, B. R., Thompson, R. A., Murphy, K. J., Nowak, R. J., Riley, C. J., Wood, W. A., Alter, S. J., and Prabhu, R., "X-33 Aerodynamic Computations and Comparisons with Wind-Tunnel Data," *Journal of Spacecraft and Rockets*, Vol. 38, No. 5, 2001, pp. 684–691.

[9]Murphy, K. J., "X-33 Hypersonic Aerodynamic Characteristics," M.S. Thesis, Dept. of Aerospace Engineering, Univ. of Texas, Austin, TX, Dec. 2000.

[10]Thompson, R. A., "Review of X-33 Hypersonic Aerodynamic and Aerothermodynamic Development," *Journal of Spacecraft and Rockets* (submitted for publication).

[11]Micol, J. R., "Experimental and Predicted Aerodynamic Characteristics of a Proposed Assured Crew Return Vehicle (ACRV) Lifting-Body Configuration," AIAA Paper 90-1403, June 1990.

[12]Brauckmann, G. J., Paulson, J. W., Jr., Weilmuenster, K. J., "Experimental and Computational Analysis of Shuttle Orbiter Hypersonic Trim Anomaly," *Journal of Spacecraft and Rockets*, Vol. 32, No. 5, 1995, pp. 758–764.

[13]Horvath, T. J., Berry, S. A., Merski, R. N., and Fitzgerald, S. M., "X-38 Experimental Aerothermodynamics," AIAA Paper 2000-2685, June 2000.

[14]Prabhu, R., "A Computational Study of an X-33 Configuration at Hypersonic Speeds," NASA CR-1999-209366, July 1999.

[15]Berry, S. A., Horvath, T. J., Hollis, B. R., Thompson, R. A., and Hamilton, H. H., II, "X-33 Hypersonic Boundary Layer Transition," *Journal of Spacecraft and Rockets*, Vol. 38, No. 5, 2001, pp. 646–657.

T. C. Lin
Associate Editor